Research Square

Preprints are preliminary reports that have not undergone peer review.
They should not be considered conclusive, used to inform clinical practice,
or referenced by the media as validated information.

Evaluation of glucoCEST MRI for assessing cerebral glucose hypometabolism in patients with Alzheimer's disease

Vasiliki Mallikourti

vasiliki.mallikourti@abdn.ac.uk

Aberdeen Biomedical Imaging Centre, School of Medicine, Medical Sciences & Nutrition, University of Aberdeen

Research Article

Keywords: Alzheimer's disease, glucose, chemical exchange saturation transfer (CEST), magnetic resonance imaging (MRI), glucoCEST, ^{18}F-FDG PET

Posted Date: September 15th, 2026

DOI: https://doi.org/10.21203/rs.3.rs-11036595/v1

License: This work is licensed under a Creative Commons Attribution 4.0 International License.
Read Full License

Additional Declarations: The authors declare no competing interests.

Abstract

Alzheimer's disease (AD) is associated with cerebral glucose hypometabolism, assessed using ^{18}F-FDG PET. Although ^{18}F-FDG PET is an established imaging modality in AD, its use is limited by cost and availability. GlucoCEST MRI has been proposed as a potential alternative. In this feasibility study, glucoCEST MRI was performed before and after oral D-glucose administration in 18 patients with AD and 18 cognitively healthy controls using a 3T MRI scanner. ^{18}F-FDG PET images were acquired in patients, with one control participant included for qualitative comparison. No significant differences in glucoCEST values were observed between groups, between pre- and post-glucose, or across cortical regions in patients (all $p > 0.05$). ^{18}F-FDG PET demonstrated significantly lower uptake in the parietal ($p = 0.045$) and temporal cortices ($p < 0.001$) compared with the frontal cortex, and these reductions were associated with lower cognition ($p < 0.01$). No associations were observed between glucoCEST signal and cognitive performance ($p > 0.05$). Bland–Altman analysis showed poor agreement between ^{18}F-FDG PET and glucoCEST in patients with AD. Machine learning using GM-masked glucoCEST features achieved an accuracy of 70.3 ± 6.1% and an AUC of 0.756 ± 0.035. These findings suggest that oral glucoCEST MRI at 3T may have limited sensitivity to detect cerebral glucose hypometabolism in AD.

Introduction

Alzheimer's disease (AD) is the most common cause of dementia, affecting approximately 10% of individuals aged ≥ 65 years, with a sharp increase in prevalence among those aged ≥ 80 years[1]. Patients experience impairments across multiple cognitive domains, including memory, language, problem-solving, activities of daily living, and executive function[2]. Although current treatments do not provide a cure, they can help manage symptoms and improve cognitive function[3]. Therefore, accurate diagnosis of AD is essential to facilitate appropriate treatment and management strategies.

Hippocampal atrophy measured by structural MRI is a recognised biomarker of AD, however, its diagnostic performance (82% sensitivity and 87% specificity) is insufficient for use as a standalone diagnostic tool[4]. AD is characterised by amyloid-β plaque accumulation and abnormal tau aggregation in the brain[5–7]. Amyloid and tau pathology can be detected using positron emission tomography (PET) with amyloid- and tau-specific radioactive tracers respectively[7,8]. However, amyloid PET has limited specificity for AD diagnosis (approximately 80%)[9] and may yield positive findings in cognitively unimpaired older adults, as the prevalence of cerebral amyloid pathology increases with age[10]. Moreover, the development of tau PET traces with highly specific binding to AD-tauopathies remains challenging[7].

Cerebral glucose hypometabolism has been observed in the temporoparietal cortices and posterior cingulate cortex in patients with early AD, with involvement of the frontal cortices as the disease progresses[8,11–13]. Glucose hypometabolism can be assessed using PET following administration of the radioactive glucose analogue 2-deoxy-2-(^{18}F)fluoro-D-glucose (^{18}F-FDG)[8,11–13]. ^{18}F-FDG is transported into cells via glucose transporters, where it undergoes phosphorylation and becomes metabolically

trapped, allowing the assessment of regional glucose metabolism. ^{18}F-FDG PET has demonstrated high diagnostic performance for differentiating AD from cognitively healthy individuals, with high sensitivity and specificity (≥ 90%)[14,15], and can also differentiate AD from other dementias[15].

Despite its diagnostic accuracy, the high cost and limited availability of PET/computed tomography (PET/CT) restrict its widespread clinical application. Furthermore, the use of radioactive tracers, combined with additional ionising radiation from CT, limits its suitability for repeated measurements. Therefore, the diagnostic assessment of AD currently involves a combination of clinical history, neurological examination, cognitive assessment, structural neuroimaging, and, where appropriate, cerebrospinal fluid (CSF) biomarker assessment. However, clinical and cognitive assessments, together with structural neuroimaging, may be inconclusive, particularly in the early stages of disease, potentially contributing to delays in diagnosis. CSF biomarkers can provide evidence of AD pathology; however, their assessment requires lumbar puncture and is therefore invasive[16]. More recently, blood-based biomarkers, particularly plasma phosphorylated tau 217 (p-tau217), have demonstrated high diagnostic accuracy for AD pathology and are increasingly being incorporated into clinical practice[17,18].

Nevertheless, blood-based and CSF biomarkers primarily provide molecular evidence of AD pathology and do not provide spatial information on brain alterations, such as the characteristic changes in cerebral glucose metabolism observed in AD. Imaging these metabolic changes may therefore provide complementary information on the location and extent of disease-related alterations within the brain.

A novel approach for imaging glucose using MRI has been developed by exploiting the interaction between hydroxyl protons in glucose and the protons in water; the method is termed glucose Chemical Exchange Saturation Transfer (glucoCEST)[19]. Glucose imaging using glucoCEST has been demonstrated on clinical 3T MRI scanners in patients with head and neck cancer[20] and brain cancer[21], supporting the feasibility for clinical translation. Furthermore, altered glucose metabolism has been detected using CEST MRI in mouse models of AD[22,23] including studies performed on clinical 3T MRI systems[22] highlighting its potential for translation to human AD studies. Unlike ^{18}F-FDG PET, glucoCEST MRI does not require radiolabelled glucose analogues, potentially facilitating future clinical implementation.

The aim of this feasibility study was to investigate the ability of glucoCEST to assess cerebral glucose hypometabolism in patients with AD. The glucoCEST sequence was first optimised using a glucose phantom. Subsequently, glucoCEST MRI was performed following oral glucose administration in patients with AD and age- and sex-matched cognitively healthy controls. GlucoCEST signal changes were compared between groups to evaluate the ability of the technique to detect disease-related differences. GlucoCEST measurements were further assessed through comparisons with ^{18}F-FDG PET uptake values and cognitive performance scores. In addition, machine learning models were employed to investigate whether glucoCEST-derived features could distinguish patients with AD from cognitively healthy controls.

Results

Phantom experiments

To optimise the CEST sequence for glucose signal measurement, phantom experiments were performed using a range of glucose concentrations. The colour maps in Fig. 1 illustrate the effect of different combinations of B_1 saturation power and saturation duration on glucose signal sensitivity. Figure 1a shows the correlation coefficient (*r*) of the linear relationship between the glucoCEST signal and glucose concentration, whereas Fig. 1b shows the corresponding slope. CEST images acquired with saturation powers between 1.5 and 2.0 μT and a saturation duration of 5 s exhibited a strong linear correlation with glucose concentration ($r \geq 0.98$), with slopes ranging from 0.39 to 0.51. These acquisition parameters provided the highest sensitivity to glucose concentration and were therefore considered optimal for subsequent *in vivo* imaging.

An example correlation plot and the corresponding CEST image from the same phantom dataset are shown in Fig. 1c and d, respectively. A strong linear correlation was observed between the glucoCEST signal and glucose concentration ($r = 0.987$, $p < 0.001$), with a measured slope of 0.39. Figure 1e presents a schematic representation of the phantom used in the study. The measurements demonstrated high reproducibility, with scan-to-scan and inter-session variability below 5% (Supplementary Tables S1 and S2).

Participant characteristics

The demographic and clinical characteristics of the participants are presented in Table 1. There were no significant differences between patients and controls in age ($p = 0.958$), fasting blood glucose levels ($p = 0.991$), or blood glucose levels following oral glucose administration ($p = 0.670$). As expected, blood glucose levels following oral glucose administration were significantly higher than fasting blood glucose levels in both groups ($p < 0.001$). Compared with controls, patients exhibited poorer cognitive performance, as reflected by significantly lower Mini-Mental State Examination (MMSE; lower scores indicate greater cognitive impairment) scores[24] and higher Alzheimer's Disease Assessment Scale–Cognitive Subscale 14-item (ADAS-Cog14; higher scores indicate greater cognitive impairment) scores[25] (both $p < 0.001$).

Table 1
Participant demographic and clinical characteristics.

N	Controls	AD patients	*p* value
	18	**18**	
Sex (M/F)	9/9	8/10	
Age (years)	72 ± 7	72 ± 8	0.958
Blood glucose levels (mM)			
Fasting glucose	5.5 ± 0.4	5.5 ± 0.4	0.991
Post oral glucose	9.1 ± 1.4	9.3 ± 1.0	0.670
Cognitive tests			
MMSE (out of 30)	28.9 ± 1.2	19.3 ± 5.5	< 0.001
ADAS Cog (out of 90)	9.8 ± 3.1	35.6 ± 19.7	< 0.001
Continuous variables are expressed as mean ± SD.			

Imaging and Cognitive Findings

Group Differences in GlucoCEST MRI Signal

No significant differences in glucoCEST values were observed between patients with AD and cognitively healthy controls across the frontal, parietal, and temporal cortices in both hemispheres (all $p > 0.05$; Fig. 2a). In addition, no significant differences were observed between baseline and post-oral glucose measurements in either group (all $p > 0.05$, Fig. 2b,c). Within patients with AD, post-glucose glucoCEST measurements did not differ significantly among the frontal, parietal, and temporal cortices ($F(1.332, 22.638) = 2.008$, $p = 0.167$, $\eta_p^2 = 0.106$, n = 18; Fig. 2d).

Representative glucoCEST images acquired from a patient with AD and a cognitively healthy control are shown in Fig. 2e. GlucoCEST images in both cases demonstrated relatively homogeneous signal distribution across the brain in both participants, with similar signal intensities observed in the frontal, parietal, and temporal cortices.

^{18}F-FDG PET Findings

Representative ^{18}F-FDG PET images acquired from the patient with AD and cognitively healthy control previously shown in Fig. 2 are presented in Fig. 3a. Compared with the healthy control participant, the patient demonstrated lower ^{18}F-FDG uptake in the bilateral temporoparietal cortices relative to the frontal

cortex. In contrast, the cognitively healthy control showed relatively preserved cortical uptake across regions.

^{18}F-FDG PET measurements differed significantly among the frontal, parietal, and temporal cortical regions ($F(2, 30) = 36.242$, $p < 0.001$, $\eta_p^2 = 0.707$, n = 16), with higher tracer uptake in the frontal cortex compared with both the parietal (1.09 ± 0.11 vs 1.01 ± 0.17, $p = 0.045$) and temporal cortices (1.09 ± 0.11 vs 0.87 ± 0.15, $p < 0.001$; Fig. 3c).

^{18}F-FDG PET measures were significantly associated with cognitive performance. After adjusting for age, MMSE scores showed positive associations with ^{18}F-FDG PET uptake in the right parietal ($\beta = 0.014$, $p = 0.038$), left parietal ($\beta = 0.020$, $p = 0.006$), and left temporal ($\beta = 0.014$, $p = 0.039$) cortices; however, only the left parietal correlation remained significant after Bonferroni correction ($p < 0.0125$, Fig. 3d). ADAS-cog scores showed significant negative associations with ^{18}F-FDG PET uptake in the left parietal ($\beta = -0.006$, $p = 0.002$) and left temporal ($\beta = -0.005$, $p = 0.006$) cortices, both of which remained significant after Bonferroni correction (Fig. 3e,f).

Relationship Between GlucoCEST MRI and ^{18}F-FDG PET

Bland–Altman analysis demonstrated poor agreement between ^{18}F-FDG PET and glucoCEST measurements across individual brain regions in each hemisphere (Fig. 4). Consistent with this finding, no significant correlations were observed between ^{18}F-FDG PET and glucoCEST measurements in the frontal, parietal, or temporal cortex in either hemisphere (all $p > 0.05$; Supplementary Fig. S1). Bar plots of ^{18}F-FDG PET and glucoCEST values for each cortical ROI in the left and right hemispheres, together with the corresponding images for each patient, are shown in Supplementary Figure S2a,b.

Relationship Between GlucoCEST MRI and Cognitive Performance

No significant correlations were observed between glucoCEST measurements and MMSE or ADAS-cog scores (all $p > 0.05$).

Machine learning Analysis

Machine learning models were used to investigate whether post-glucose glucoCEST images could distinguish patients with AD from cognitively healthy controls. Classification performance was assessed using receiver operating characteristic (ROC) analysis and the area under the curve (AUC), together with accuracy, precision, recall, and F1-score. Performance was compared between models trained on whole-brain post-glucose glucoCEST images and GM-masked post-glucose glucoCEST images. Classification performance metrics are summarised in Table 2.

Table 2
Classification performance of machine learning models using post-glucose whole-brain and grey matter (GM)-restricted glucoCEST image features.

Dataset	Group	AUC	Accuracy (%)	Precision (%)	Recall (%)	F1-score (%)
Post-glucose whole brain glucoCEST	Controls		84.3 ± 6.2	85.4 ± 10.1	85.3 ± 7.1	84.8 ± 5.4
	Patients	0.934 ± 0.028		85.3 ± 05.8	83.5 ± 13.3	83.6 ± 7.4
Post-glucose GM glucoCEST	Controls		70.3 ± 6.1	70.5 ± 6.8	72.4 ± 13.9	70.3 ± 8.0
	Patients	0.756 ± 0.035		72.4 ± 07.9	68.7 ± 12.0	69.5 ± 6.5

The whole-brain post-glucose glucoCEST model achieved higher classification performance compared with the GM-masked model across all evaluated performance metrics. The whole-brain model achieved an AUC of 0.934 ± 0.028 compared with 0.756 ± 0.035 for the GM-masked model (ROC curves shown in Fig. 5). Classification accuracy was also higher for the whole-brain model compared with the GM-masked model (84.3 ± 6.2% vs 70.3 ± 6.1%, respectively). Similarly, the whole-brain model demonstrated higher precision, recall, and F1-score values compared with the GM-masked model.

Class-wise analysis showed balanced performance between controls and patients for the whole-brain model, with comparable recall, precision, and F1-score values across both groups. In comparison, the GM-masked model showed lower classification performance for both groups, while maintaining a similar pattern between control and patient metrics.

Discussion

In this feasibility study, glucoCEST, an MRI-based technique, was evaluated as a potential alternative imaging technique to ^{18}F-FDG PET for detecting cerebral glucose hypometabolism in individuals with AD. In contrast to PET, which requires intravenous ^{18}F-FDG glucose administration and exposes patients to ionising radiation, this study employed a fully non-invasive approach in which participants consumed a D-glucose-containing drink prior to scanning. GlucoCEST MRI signal changes were compared between patients with AD and cognitively healthy control participants. The performance of glucoCEST was then assessed through comparisons with ^{18}F-FDG PET-derived glucose uptake measurements, cognitive performance scores, and machine learning-based classification models.

GlucoCEST MRI did not demonstrate clear regional differences in glucose signal between patients with AD and cognitively healthy participants. Specifically, no consistent differences were observed in the parietal, temporal, or frontal cortices under the post-glucose condition. In addition, no measurable change in glucoCEST signal was observed between pre- and post-glucose measurements in either

patients with AD or cognitively healthy controls. These findings may indicate limited sensitivity of the current protocol to detect glucose-related signal alterations and to distinguish patients with AD from cognitively healthy controls under the applied conditions.

^{18}F-FDG PET imaging in patients with AD demonstrated a relative reduction in glucose uptake in temporoparietal regions compared with frontal cortical regions, consistent with the characteristic pattern of Alzheimer's disease[8,11,26]. The ^{18}F-FDG PET scan from a cognitively healthy control participant provided a qualitative reference for the expected cortical metabolic pattern, rather than being used for statistical comparison. Furthermore, ^{18}F-FDG PET signal in these regions showed a relationship with cognitive scores, such that lower metabolic activity was associated to cognitive decline, consistent with literature[13].

When compared with ^{18}F-FDG PET, glucoCEST signal values showed no clear correspondence across the regions tested, as supported by Pearson correlation and Bland–Altman analyses. These findings suggest limited agreement between the two modalities under the current implementation, indicating that glucoCEST may not directly reflect ^{18}F-FDG PET measures of cerebral glucose metabolism in AD. Moreover, no clear association was observed between glucoCEST signal measures and cognitive performance scores, indicating a lack of correspondence between imaging-derived metabolic signal and clinical cognitive function in this cohort.

Machine learning analyses further supported these findings. While classification using whole-brain post-glucose glucoCEST images demonstrated high accuracy and discriminative performance, restricting the feature space to GM regions was associated with reduced classification accuracy and AUC. These findings suggest that the discriminative information captured by the model may extend beyond regional GM-restricted glucose signal changes, with whole-brain images providing additional features that contribute to improved separation between patients with AD and cognitively healthy controls.

Although previous studies have reported increased hippocampal glucose concentration following oral glucose administration in patients, due to the impaired cellular glucose metabolism[27], our findings indicate that post-glucose signal changes may have been too small to be reliably detected using the current glucoCEST methodology. Several factors may account for these findings, including the inherently low signal-to-noise ratio of glucoCEST at clinical field strengths, physiological variability in glucose uptake following oral administration, and residual partial volume effects at tissue boundaries despite CSF masking and cortical restriction. In addition, cortical atrophy and structural variability in AD may have contributed to the observed inter-subject variability in glucoCEST measurements. Intravenous glucose administration, as have been used in brain cancer studies[20,21,28], may therefore offer a more sensitive alternative for future investigations. Motion artefacts represented a particular challenge in the AD cohort and resulted in the exclusion of several datasets. This highlights the practical difficulties of acquiring glucoCEST scans in cognitively impaired populations and suggests that shorter acquisition protocols may be preferable in this population. Nevertheless, given the feasibility design and relatively small sample size, these findings require confirmation in larger studies.

This study provides a multimodal assessment of glucoCEST MRI in AD, incorporating regional imaging analysis, ^{18}F-FDG PET as a metabolic reference, cognitive performance measures, and machine learning. Importantly, this work represents an early step in the evaluation of glucoCEST MRI as a potential non-ionising alternative to ^{18}F-FDG PET imaging for assessing cerebral glucose hypometabolism in AD. In principle, MRI-based techniques offer practical advantages over PET imaging, including wider availability, reduced patient burden, and the absence of ionising radiation. While these results do not support clinical utility in its current form, they provide a valuable foundation for further methodological development and optimisation of CEST MRI-based approaches for brain metabolic imaging in dementia.

In conclusion, glucoCEST values did not demonstrate strong associations with ^{18}F-FDG PET glucose uptake measures or cognitive scores and did not distinguish patients with AD from cognitively healthy controls. These findings suggest that, under the conditions tested, including oral glucose administration and imaging on a clinical 3 T MRI system, glucoCEST may have limited sensitivity for detecting cerebral glucose hypometabolism in AD. Further studies using alternative glucose delivery strategies, including intravenous glucose administration, and/or higher field strengths, such as 7 T, are needed to determine its potential for assessing cerebral glucose metabolism.

Methods

The study was approved by the London Southeast Research Ethics Committee (22/LO/0347), and all procedures were conducted in accordance with the Declaration of Helsinki guidelines. All participants or their representatives provided written informed consent prior to the study.

MRI images were acquired on a clinical 3 T MRI scanner (Achieva, dStream, Philips, Netherlands) using a 32-channel head coil for signal reception.

Phantom experiments

Ten plastic tubes were arranged in a circular holder and filled with 9 g/L sodium chloride, 0.468 mM copper sulphate (to match human brain T_1), and D-glucose at concentrations of 1–10 mM. While pH was not measured, the constant copper sulphate concentration likely minimised pH variability, making glucose the primary variable affecting the glucoCEST signal.

CEST images were acquired using a turbo spin echo sequence with matrix size of 256 x 256, voxel size of 0.9 x 0.9 x 6 mm, FOV = 230 x 201 x 18 mm, repetition time (TR)/ echo time (TE) of 6442/ 8.3 ms, excitation/refocusing flip angle of $90^0/120^0$, turbo factor of 170, three slices, and saturation frequency offsets at ± 1.2, ± 2.1, ± 3.0, and − 1560 ppm (S0). The image acquisition was repeated three times at + 2.1 ppm with different echo shifts including a total of nine Z-spectral images. Various B_1 saturation powers (0.6, 1.0, 1.17, 1.5, 1.6, 1.7, 2.0 μT) and saturation times (0.5, 0.9, 1.5, 2.0, 2.5, 3.0, 5 s) were applied to allow optimisation of the CEST pre-pulse.

The reproducibility of the optimised sequence was evaluated by performing five repeated acquisitions on the same day and two acquisitions on separate days within a one-week period.

Data were processed using in-house scripts written in MATLAB (MathWorks, Natick, MA, USA). The glucoCEST images were reconstructed with intrinsic B_0 correction[29] and exported directly from the scanner. Circular regions of interests (ROIs) with a radius of 10 pixels were automatically generated for each tube, and the mean signal within each ROI was extracted for analysis.

Human experiments

Participants

Twenty-one participants aged ≥ 60 years with a clinical diagnosis of AD and 25 age- and sex-matched cognitively healthy controls without AD were recruited between December 2023 and September 2024. Patients were recruited via local general practitioner (GP) databases, the NHS Research Scotland Neuroprogressive and Dementia Network, and local memory clinics at Aberdeen Royal Infirmary. Healthy controls were recruited through GP databases, the NHS Research Scotland Neuroprogressive and Dementia Network, and public advertisements. Clinical diagnosis of AD was based on the criteria of the National Institute on Ageing and Alzheimer's Association[30]. The patients had been diagnosed by experiences clinicians working in the dementia field and diagnoses were reviewed before enrolment. Controls were eligible if they reported no subjective memory complaints and demonstrated normal cognitive performance, defined as an MMSE score ≥ 24 and an ADAS-Cog score within the normal range. Individuals with a family history of AD were excluded from the control group to minimise potential genetic risk confounding. Across both groups, exclusion criteria included a history of diabetes, major stroke, or any contraindications to MRI.

Following screening, two patients and five controls were excluded due to elevated fasting blood glucose levels (> 6.1 mmol/L). One patient was excluded because kyphosis prevented MRI scanning in the supine position, and two controls were excluded due to technical issues affecting data analysis. The final study cohort comprised 18 patients with AD (mean age, 72 ± 8 years; age rage, 62–90 years) and 18 cognitively healthy controls (mean age, 72 ± 7 years; age rage, 62–84 years) (Supplementary Fig. S3a).

Participants

Twenty-one participants aged ≥ 60 years with a clinical diagnosis of AD and 25 age- and sex-matched cognitively healthy controls without AD were recruited between December 2023 and September 2024. Patients were recruited via local general practitioner (GP) databases, the NHS Research Scotland Neuroprogressive and Dementia Network, and local memory clinics at Aberdeen Royal Infirmary. Healthy controls were recruited through GP databases, the NHS Research Scotland Neuroprogressive and Dementia Network, and public advertisements. Clinical diagnosis of AD was based on the criteria of the

National Institute on Ageing and Alzheimer's Association[30]. The patients had been diagnosed by experiences clinicians working in the dementia field and diagnoses were reviewed before enrolment. Controls were eligible if they reported no subjective memory complaints and demonstrated normal cognitive performance, defined as an MMSE score ≥ 24 and an ADAS-Cog score within the normal range. Individuals with a family history of AD were excluded from the control group to minimise potential genetic risk confounding. Across both groups, exclusion criteria included a history of diabetes, major stroke, or any contraindications to MRI.

Study procedures

Participants underwent an overnight fast prior to imaging. On arrival, blood glucose levels were measured using a finger-prick test to confirm eligibility. Participants then underwent baseline MRI acquisition including a T_1-weighted image and glucoCEST scans. Following completion of the baseline scan, the table was withdrawn, the participant stood up to ingest 75 g of D-glucose dissolved in 113 mL of solution (Polycal Neutral Liquid). The participant was then repositioned in the scanner, and post-glucoCEST imaging along with a T_1_weighted image were acquired continuously from 2 to 42 minutes following ingestion. After MRI acquisition, the participant's blood glucose level was measured again using a finger-prick test. Subsequently, participants completed two cognitive assessments: the MMSE and the ADAS-Cog to assess cognitive performance. Sixteen of the 18 patients with AD and one healthy control additionally underwent ^{18}F-FDG PET imaging approximately one week later, with the PET images from the cognitively healthy control used for qualitative comparison (Supplementary Fig. S3b).

Four baseline glucoCEST scans were acquired for the first three patients and the first control participant as part of the initial protocol. Following protocol optimisation, a single baseline scan was acquired for the subsequent 14 patients and 17 control participants. Baseline glucoCEST scan was not acquired for one patient due to an acquisition oversight during the imaging session. The imaging protocol included thirteen post-glucose glucoCEST scans for the first three patients and twelve post-glucose scans for the remaining patients. Seven patients were unable to complete the full scanning protocol, resulting in incomplete post-glucose datasets. Up to thirteen post-glucose glucoCEST scans were acquired for controls.

Image acquisition

High-resolution 3D T1-weighted images were obtained pre and post oral glucose administration using a three-dimensional gradient echo sequence with matrix size of 256 x 256, voxel size of 0.67 x 0.67 x 0.67, TR of 8.21 ms, TE of 3.77 ms, TI of 950 ms, and flip angle of 8.

The glucoCEST images were acquired using same sequence parameters as in phantoms with B_1 saturation powers of 1.5 μT and saturation time of 5 s. Three slices were acquired starting at the level of

the anterior commissure–posterior commissure (AC–PC) line and extending superiorly. Scan duration was 1:11 minutes.

^{18}F-FDG PET/CT images were acquired on a GE Discovery 710 scanner. Dynamic ^{18}F-FDG PET data were acquired as 4 five-minute frames over 20 minutes after an intravenous bolus injection of 250 Mbq. The uptake period between injection and scanning was 30 minutes.

Image analysis

Data were processed using in-house scripts written in MATLAB (MathWorks, Natick, MA, USA). Motion correction of the Z-spectral images was performed using MCFLIRT[31] in FSL (version 6.0.7; FMRIB Software Library, Oxford, UK)[32], with the 2.1 ppm image used as the reference volume. The images were subsequently denoised using a non-local means (NLM) filter[33,34]. Then, the Z-spectra were normalised by dividing the images acquired with off-resonance saturation pulses by the unsaturated reference image (S_0 at − 1560 ppm) and interpolated using a multipool Lorentzian fitting method containing a magnetisation transfer pool (Frequency − 2.4 ppm, width 10.0 ppm), an amide pool (Frequency 3.5 ppm, width 0.5 ppm) and two nuclear Overhauser effect pools (Frequency − 1.0 ppm, width 2.0 ppm; Frequency − 2.6 ppm, width 1.0 ppm) as well as the glucose pool at 2.1 ppm[34]. The intrinsic B_0 map acquired by the scanner as part of the CEST sequence was used for voxel-wise B_0 inhomogeneity correction. Following B_0 correction, glucose-weighted contrast was quantified using magnetisation transfer ratio asymmetry (MTR_{asym}) analysis, calculated as:

$$MTR_{asym}(\Delta\omega) = \frac{S(-\Delta\omega) - S(+\Delta\omega)}{S_0}$$

where $S(+\Delta\omega)$ and $S(-\Delta\omega)$ denote the normalised signal intensities at positive and negative frequency offsets, respectively, and S_0 is the unsaturated reference signal.

MTR_{asym} images with excessive motion that could not be adequately corrected were excluded from further analysis.

Due to participant repositioning between MRI scans, separate preprocessing pipelines were implemented for the pre- and post-oral glucose administration datasets using Statistical Parametric Mapping (SPM12) and MATLAB (Fig. 6). Automated ROIs were defined using two anatomical atlases. The BCI-DNI anatomical brain atlas[35] was used to define ROIs within the frontal, parietal, and temporal lobes, while the Harvard–Oxford Atlas was used to define ROIs in the thalamus. The SPM grey matter (GM) probability mask was applied to the BCI-DNI atlas to restrict the analysis to cortical tissue. Both atlases were inversed normalised from MNI space to each participant's image space and co-registered to each MTR_{asym} image within that participant.

T_1-weighted images were coregistered to each participant's MTR_{asym} image. Automated image segmentation for cerebrospinal fluid (CSF) was subsequently performed on the coregistered T_1-weighted images. The resulting CSF mask was used to exclude CSF voxels from the MTR_{asym} images. Binary ROI masks were then applied to the CSF-corrected MTR_{asym} images. ROIs were extracted separately for the left and right hemispheres. Median glucoCEST values were calculated within ROI. For each participant, glucoCEST values were averaged across baseline scans and separately across post-glucose scans. The resulting values were then normalised to the corresponding averaged glucoCEST value measured in the thalamus, as the thalamus is relatively preserved in AD[8,26].

For comparison purposes, same ROIs were extracted from the ^{18}F-FDG PET images. Dynamic ^{18}F-FDG PET images from each participant were averaged across four time points and the resulting averaged image was normalised to the standard MNI template in SPM12. Thalamus ROI was extracted from the AAL atlas[36]. Lobar ROIs were extracted from the BCI-DNI anatomical brain atlas[35], with a GM mask applied to restrict analyses to cortical tissue. ROIs were defined separately for the left and right hemispheres. Mean PET uptake values were extracted from each ROI and normalised to the corresponding thalamic uptake.

Statistical analysis

Statistical analysis was performed in SPSS (IBM Corp). Data normality was evaluated using the Shapiro–Wilk test. Continuous variables, including demographic data, memory scores and blood glucose levels were expressed as mean ± SD. Demographical differences between groups were assessed using t-tests or Mann Whitney-U tests for normally or non-normally distributes data, respectively.

Linear regression analysis was used to evaluate and optimise the CEST acquisition parameters. For each acquisition condition (combination of saturation power and saturation duration), the slope of the regression line between the glucoCEST signal and glucose concentration was calculated to assess sensitivity, while the Pearson correlation coefficient (r) was used to quantify linearity.

Differences in glucoCEST values between patients with AD and cognitively healthy controls were assessed using independent-samples t-tests for normally distributed data and Mann–Whitney U tests for non-normally distributed data. Differences between pre- and post-oral glucose measurements were assessed using paired-samples t-tests for normally distributed data and Wilcoxon signed-rank tests for non-normally distributed data. Linear regression analysis was used to assess associations between imaging measures and cognitive performance scores corrected for age. Bonferroni correction was applied to account for multiple comparisons (number of ROIs) with statistical significance defined as $p < 0.0083$. Regional ^{18}F-FDG PET and glucoCEST values across the frontal, parietal, and temporal cortices were compared in patients using repeated-measures ANOVA with statistical significance defined as $p < 0.05$. All statistical tests were two sided.

Finally, agreement between ^{18}F-FDG PET and glucoCEST measurements was assessed using Bland–Altman analysis for each cortical ROI to estimate bias and limits of agreement. Associations between ^{18}F-FDG PET and glucoCEST measurements were further evaluated using Pearson correlation analysis, performed separately for each hemisphere and cortical region.

Machine Learning Analysis

Two independent machine learning pipelines were evaluated to assess the classification performance of post-glucose glucoCEST MRI data. The first pipeline used whole-brain glucoCEST images as input, whereas the second pipeline applied a GM tissue probability mask to restrict analysis to GM regions, enabling comparison between whole-brain and GM-specific image features.

Identical preprocessing was applied to both pipelines. Image slices were extracted from each scan, and pixel intensities were normalised to the range 0–1 using the MinMaxScaler function implemented in scikit-learn. Images were resized to 224 × 224 pixels to match the input requirements of the feature extraction model. Feature extraction was performed using a pre-trained Distilled Data-efficient Image Transformer (DeiT) model (DeiT-base distilled patch16-224) based on the Vision Transformer (ViT) architecture[37]. Each image slice was represented by a 768-dimensional feature vector corresponding to the learned class (CLS) embedding generated by the network. The extracted feature vectors were used to train a support vector machine (SVM) classifier with a linear kernel (C = 1.0) to distinguish patients with Alzheimer's disease (AD) from cognitively healthy controls. Classification performance was evaluated using stratified 5-fold cross-validation performed at the subject level, preserving the proportion of AD patients and cognitively healthy controls in each fold. The same subject-level splits were applied to both pipelines to enable direct comparison.

Model performance was assessed using ROC curve analysis and AUC. Accuracy, precision, recall, and F1-score were calculated to further characterise classifier performance.

Data availability

The datasets generated and/or analysed during the current study are available from the corresponding author on reasonable request.

Declarations

Acknowledgements

The author would like to thank the research nurses Mrs Ruth Valentine and Mrs Julie Scott for supporting patient recruitment, conducting patient consent, and conducting the cognitive tests, Ms Amanda Cardy for supporting participant recruitment through GP databases, the radiographers Mr

Michael Hendry, Ms Laura Reid, Mrs Michelle Mauchline, Mr Arthur Ginsburg, Mrs Sian Lindsey for data acquisition, Dr Matthew Clemence (Philips Healthcare Clinical Science, UK) for scanner methods support, Mrs Teresa Morris and Mrs Dawn Younie for logistic support, and Dr Celia Gabriela Alvarez for her advice regarding research ethics. This project has received funding from Chief Scientist Office (CSO) under grant number TCS/21/03.

Author contributions

V.M. contributed to the study conceptualisation, funding and design, conducted data and statistical analysis, constructed the figures, and contributed to the writing of the original manuscript; A.A.G. conducted the AI analysis and contributed to the writing ; H.S.A.S. conducted data and statistical analysis for phantom experiments; N.S. supported the MRI protocol setup and data processing; J.M. performed patient recruitment; P.M. contributed to the study funding and design; G.D.W. contributed to the study conceptualisation, funding and design, supervised the research, and conducted data processing. All Authors have reviewed and approved the submitted version.

Additional Information

The authors declare no competing interests.

References

1. Kukull WA et al (2002) Dementia and Alzheimer Disease Incidence: A Prospective Cohort Study. Arch Neurol 59:1737
2. Huang Y, Mucke L (2012) Alzheimer Mechanisms and Therapeutic Strategies. Cell 148:1204–1222
3. Hampel H et al (2018) The cholinergic system in the pathophysiology and treatment of Alzheimer's disease. Brain 141:1917–1933
4. Park HY, Suh CH, Heo H, Shim WH, Kim SJ (2022) Diagnostic performance of hippocampal volumetry in Alzheimer's disease or mild cognitive impairment: a meta-analysis. Eur Radiol 32:6979–6991
5. Thal DR, Rüb U, Orantes M, Braak H (2002) Phases of Aβ-deposition in the human brain and its relevance for the development of AD. Neurology 58:1791–1800
6. Mattson MP (2004) Pathways towards and away from Alzheimer's disease. Nature 430:631–639
7. Leuzy A et al (2019) Tau PET imaging in neurodegenerative tauopathies—still a challenge. Mol Psychiatry 24:1112–1134
8. Marcus C, Mena E, Subramaniam RM (2014) Brain PET in the Diagnosis of Alzheimer's Disease. Clin Nucl Med 39:e413–e426
9. Ruan D, Sun L (2023) Amyloid-β PET in Alzheimer's disease: A systematic review and Bayesian meta-analysis. Brain Behav 13:e2850

10. Jansen WJ et al (2015) Prevalence of Cerebral Amyloid Pathology in Persons Without Dementia: A Meta-analysis. JAMA 313:1924
11. Nordberg A, Rinne JO, Kadir A, Långström B (2010) The use of PET in Alzheimer disease. Nat Rev Neurol 6:78–87
12. Siebner H et al (2003) Cerebral metabolic changes accompanying conversion of mild cognitive impairment into Alzheimer's disease: a PET follow-up study. Eur J Nucl Med Mol Imaging 30:1104–1113
13. Mosconi L et al (2009) FDG-PET changes in brain glucose metabolism from normal cognition to pathologically verified Alzheimer's disease. Eur J Nucl Med Mol Imaging 36:811–822
14. Bloudek LM, Spackman DE, Blankenburg M, Sullivan SD (2011) Review and Meta-Analysis of Biomarkers and Diagnostic Imaging in Alzheimer's Disease. J Alzheimer's Dis 26:627–645
15. Mosconi L et al (2008) Multicenter Standardized^{18} F-FDG PET Diagnosis of Mild Cognitive Impairment, Alzheimer's Disease, and Other Dementias. J Nucl Med 49:390–398
16. Tapiola T et al (2009) Cerebrospinal Fluid β-Amyloid 42 and Tau Proteins as Biomarkers of Alzheimer-Type Pathologic Changes in the Brain. Arch Neurol 66
17. Ashton NJ et al (2024) Diagnostic Accuracy of a Plasma Phosphorylated Tau 217 Immunoassay for Alzheimer Disease Pathology. JAMA Neurol 81:255
18. Palmqvist S et al (2024) Blood Biomarkers to Detect Alzheimer Disease in Primary Care and Secondary Care. JAMA 332:1245
19. Ward KM, Aletras AH, Balaban RS (2000) A New Class of Contrast Agents for MRI Based on Proton Chemical Exchange Dependent Saturation Transfer (CEST). J Magn Reson 143:79–87
20. Wang J et al (2016) Magnetic Resonance Imaging of Glucose Uptake and Metabolism in Patients with Head and Neck Cancer. Sci Rep 6:30618
21. Wu Y et al (2023) Improved postprocessing of dynamic glucose-enhanced CEST MRI for imaging brain metastases at 3 T. Eur Radiol Exp 7:78
22. Huang J et al (2020) Altered d -glucose in brain parenchyma and cerebrospinal fluid of early Alzheimer's disease detected by dynamic glucose-enhanced MRI. Sci Adv 6:eaba3884
23. Tolomeo D et al (2018) Chemical exchange saturation transfer MRI shows low cerebral 2-deoxy-D-glucose uptake in a model of Alzheimer's Disease. Sci Rep 8:9576
24. Folstein MF, Folstein SE, McHugh PR (1975) Mini-mental state: A practical method for grading the cognitive state of patients for the clinician. J Psychiatr Res 12:189–198
25. Kueper JK, Speechley M, Montero-Odasso M (2018) The Alzheimer's Disease Assessment Scale–Cognitive Subscale (ADAS-Cog): Modifications and Responsiveness in Pre-Dementia Populations. A Narrative Review. J Alzheimer's Dis 63:423–444
26. Mosconi L (2005) Brain glucose metabolism in the early and specific diagnosis of Alzheimer?s disease: FDG-PET studies in MCI and AD. Eur J Nucl Med Mol Imaging 32:486–510

27. Haley AP, Knight-Scott J, Simnad VI, Manning CA (2006) Increased glucose concentration in the hippocampus in early Alzheimer's disease following oral glucose ingestion. Magn Reson Imaging 24:715–720
28. Xu X et al (2015) Dynamic Glucose-Enhanced (DGE) MRI: Translation to Human Scanning and First Results in Glioma Patients. Tomography 1:105–114
29. Togao O et al (2017) Amide proton transfer imaging of brain tumors using a self-corrected 3D fast spin-echo dixon method: comparison with separate B0 correction. Magn Reson Med 77:2272–2279
30. McKhann GM et al (2011) The diagnosis of dementia due to Alzheimer's disease: Recommendations from the National Institute on Aging-Alzheimer's Association workgroups on diagnostic guidelines for Alzheimer's disease. Alzheimers Dement 7:263–269
31. Jenkinson M, Bannister P, Brady M, Smith S (2002) Improved Optimization for the Robust and Accurate Linear Registration and Motion Correction of Brain Images. NeuroImage 17:825–841
32. Woolrich MW et al (2009) Bayesian analysis of neuroimaging data in FSL. *NeuroImage* 45, S173–S186
33. Buades A, Coll B, Morel J-MA, Non-Local Algorithm for Image Denoising. in (2005) *IEEE Computer Society Conference on Computer Vision and Pattern* Recognition *(CVPR'05)* vol. 2 60–65 (IEEE, San Diego, CA, USA, 2005)
34. Wittsack H-J, Radke KL, Stabinska J, Ljimani A (2023) Müller-Lutz, A. calf – Software for CEST Analysis with Lorentzian Fitting. J Med Syst 47:39
35. Joshi AA et al (2022) A hybrid high-resolution anatomical MRI atlas with sub-parcellation of cortical gyri using resting fMRI. J Neurosci Methods 374:109566
36. Rolls ET, Huang C-C, Lin C-P, Feng J, Joliot M (2020) Automated anatomical labelling atlas 3. *NeuroImage* 206, 116189
37. Touvron H, Cord M, Douze M, Massa F, Sablayrolles A, Jégou Hervé (2021) Training data-efficient image transformers & distillation through attention. in *Proceedings of Machine Learning Research* vol. 139 10347–10357

Figures

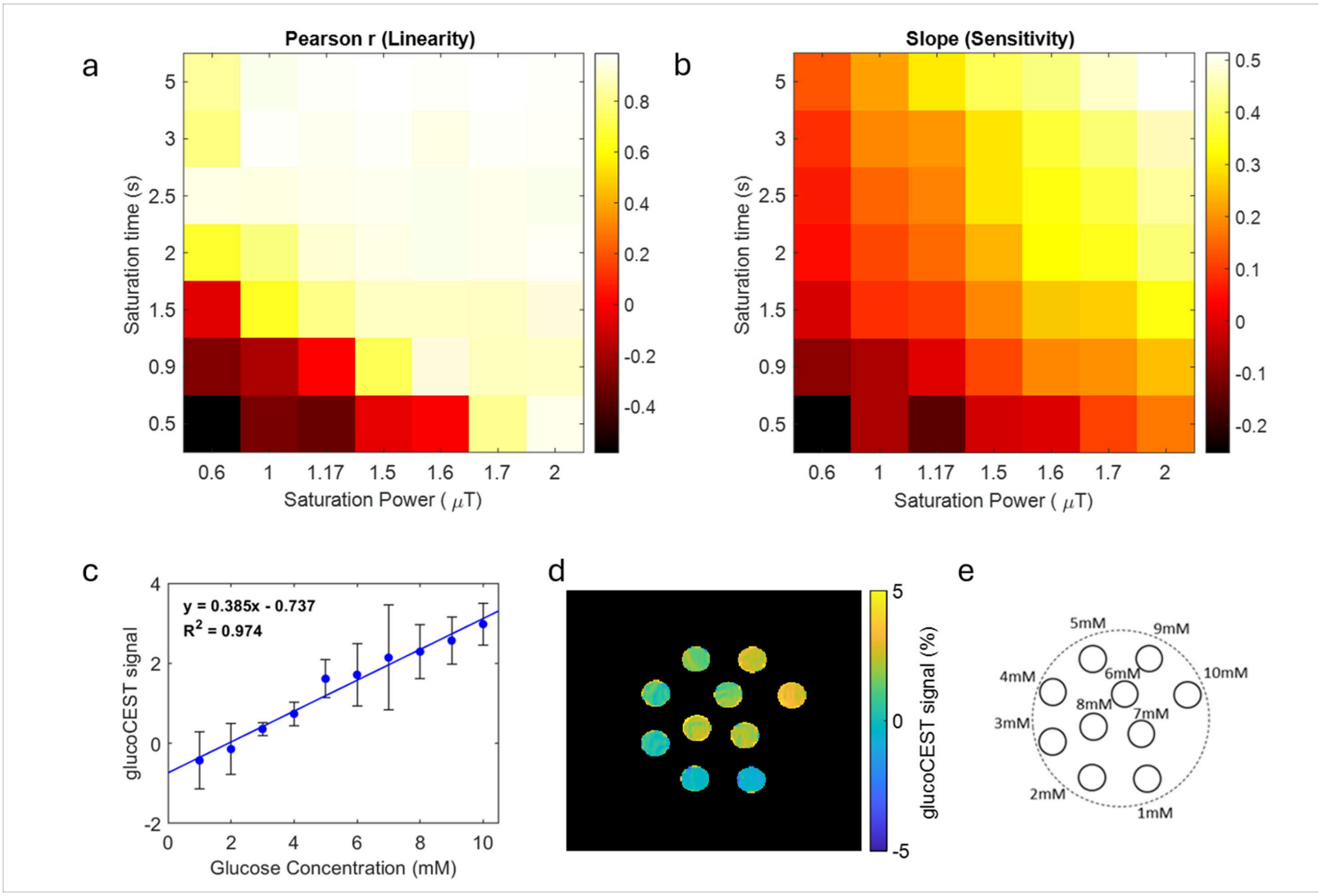


Figure 1

Optimisation of glucoCEST acquisition parameters using phantom experiments. (a) Colour map of correlation coefficient (*r*) derived from linear fitting between glucoCEST signal and glucose concentration indicating linearity, (b) Colour map of the corresponding slope indicating method sensitivity, (c) Example correlation plot showing the relationship between glucose concentration and glucoCEST signal in phantom, (d) corresponding glucoCEST image of the phantom, and (e) schematic illustration of the phantom experimental setup.

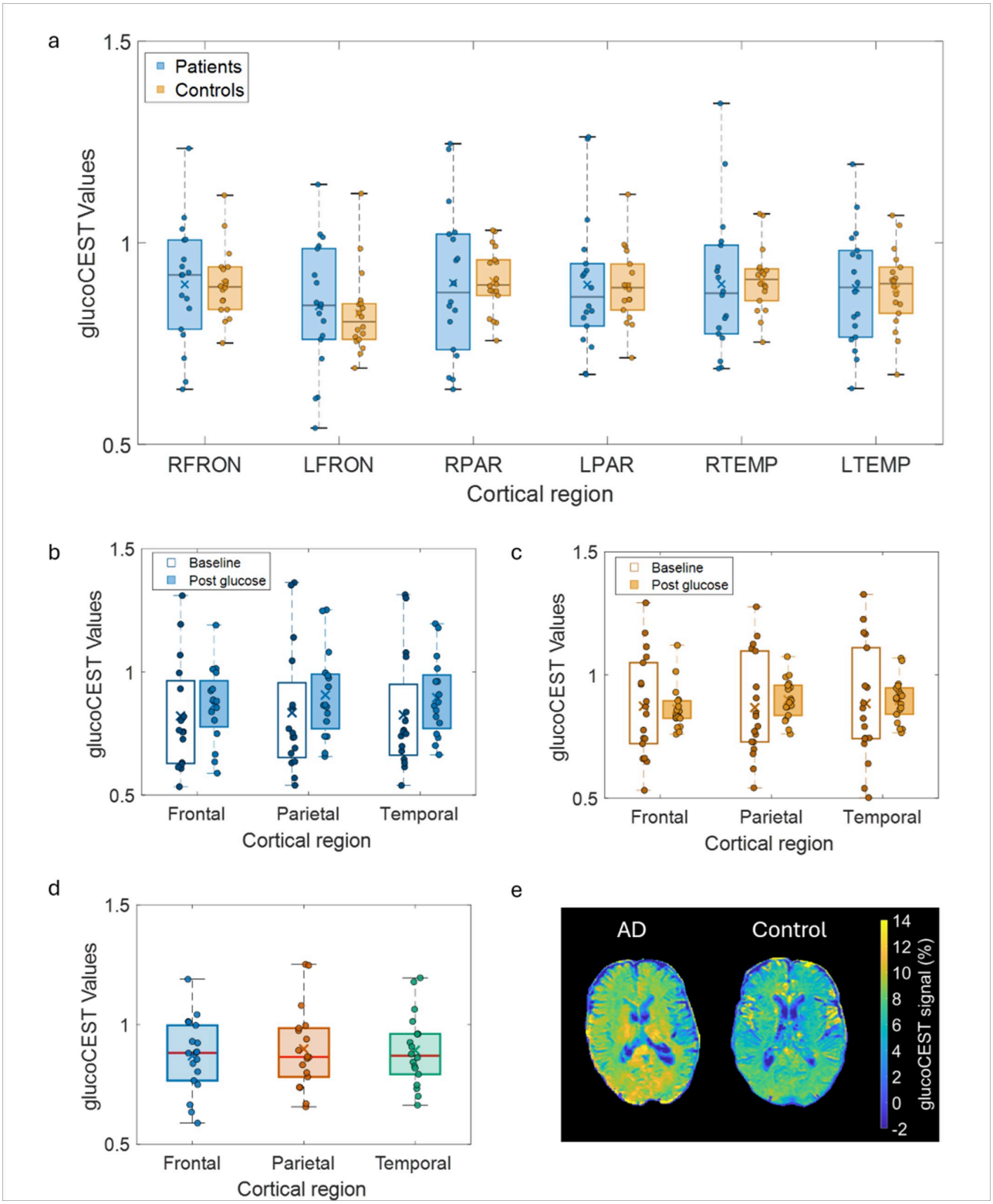


Figure 2

GlucoCEST MRI findings. Box plots show (a) the comparison of post-glucose glucoCEST signal between patients with AD and cognitively healthy controls (n = 18 per group), (b) the comparison of glucoCEST signal between baseline and following oral glucose administration in patients with AD (n = 16), (c) the comparison of glucoCEST signal between baseline and following oral glucose administration in cognitively healthy controls (n = 18), and (d) the distribution of post-glucose glucoCEST values across

the frontal, parietal, and temporal cortical regions in patients with AD (n = 18). Individual data points representing the glucoCEST value for the corresponding tissue ROI are overlaid for each participant. (e) Representative glucoCEST images from a 69-year-old female participant with AD and a 71-year-old female cognitively healthy control. RFRON = right frontal cortex, LFRON = left frontal cortex, RPAR = right parietal cortex, LPAR = left parietal cortex, RTEMP = right temporal cortex, LTEMP = left temporal cortex.

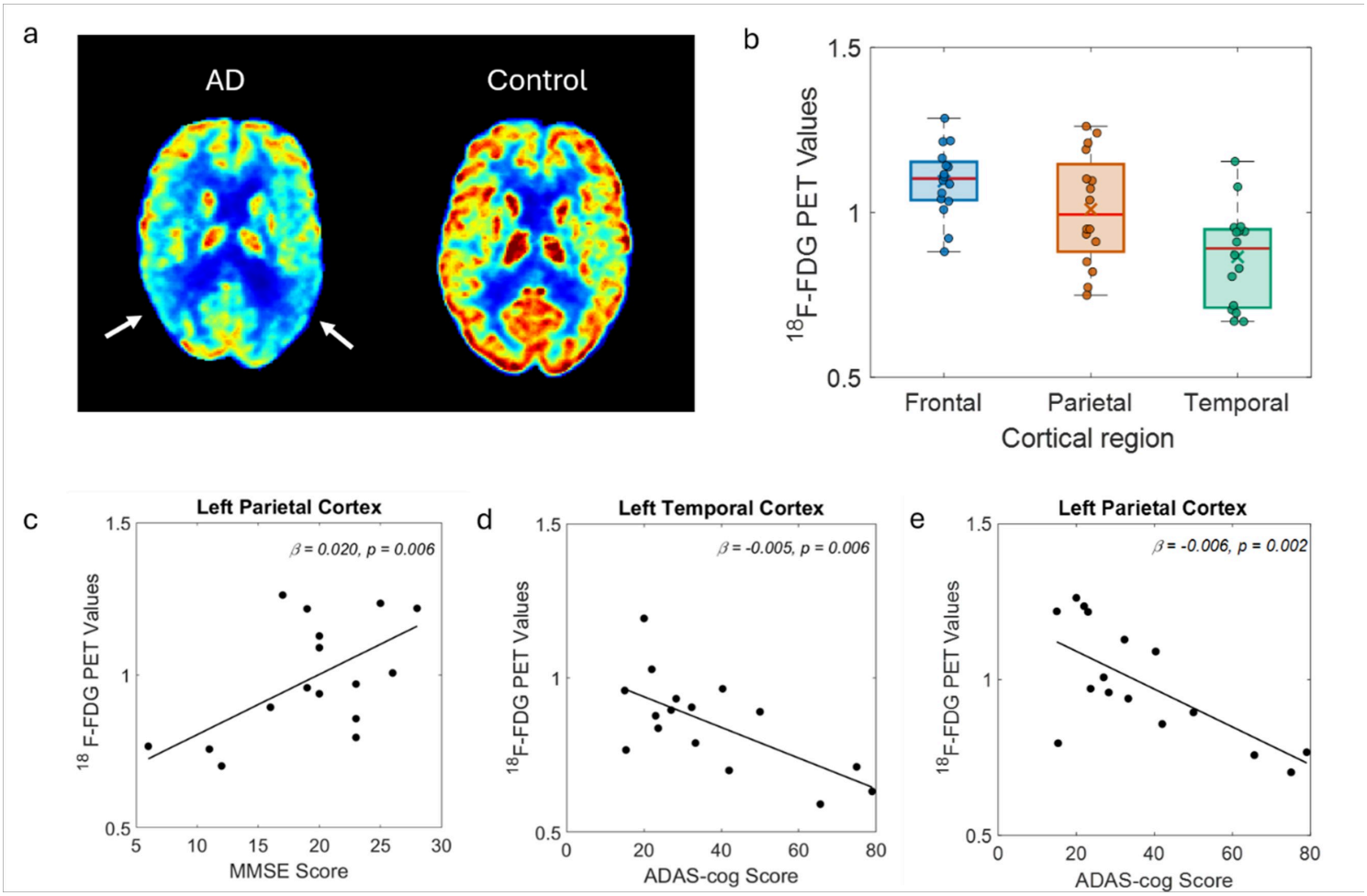


Figure 3

¹⁸F-FDG PET findings. (a) Representative ¹⁸F-FDG-PET image from a participant with AD and a cognitively healthy control participant shown in Figure 2. Images are displayed using raw FDG uptake values. The arrows indicate areas of reduced glucose uptake in the AD participant, particularly in the bilateral temporal and parietal cortices, compared with the control participant. (b) Box plots show the distribution of ¹⁸F-FDG-PET values across the frontal, parietal, and temporal cortical regions in patients with AD (n = 16). Individual data points are overlaid for each participant. (c) Linear regression analysis between ¹⁸F-FDG-PET values and MMSE scores in the left parietal cortex. (d) Linear regression analysis between ¹⁸F-FDG-PET values and ADAS-Cog scores in the left parietal cortex. (e) Linear regression analysis between ¹⁸F-FDG-PET values and ADAS-Cog scores in the left temporal cortex. Each point represents the mean value across the corresponding tissue ROI in one patient (n = 16). Each plot shows the regression line, with the corresponding regression slope (β) and p-value displayed. Linear

regressions were adjusted for age, and *p*-values were corrected for multiple comparisons using the Bonferroni method.

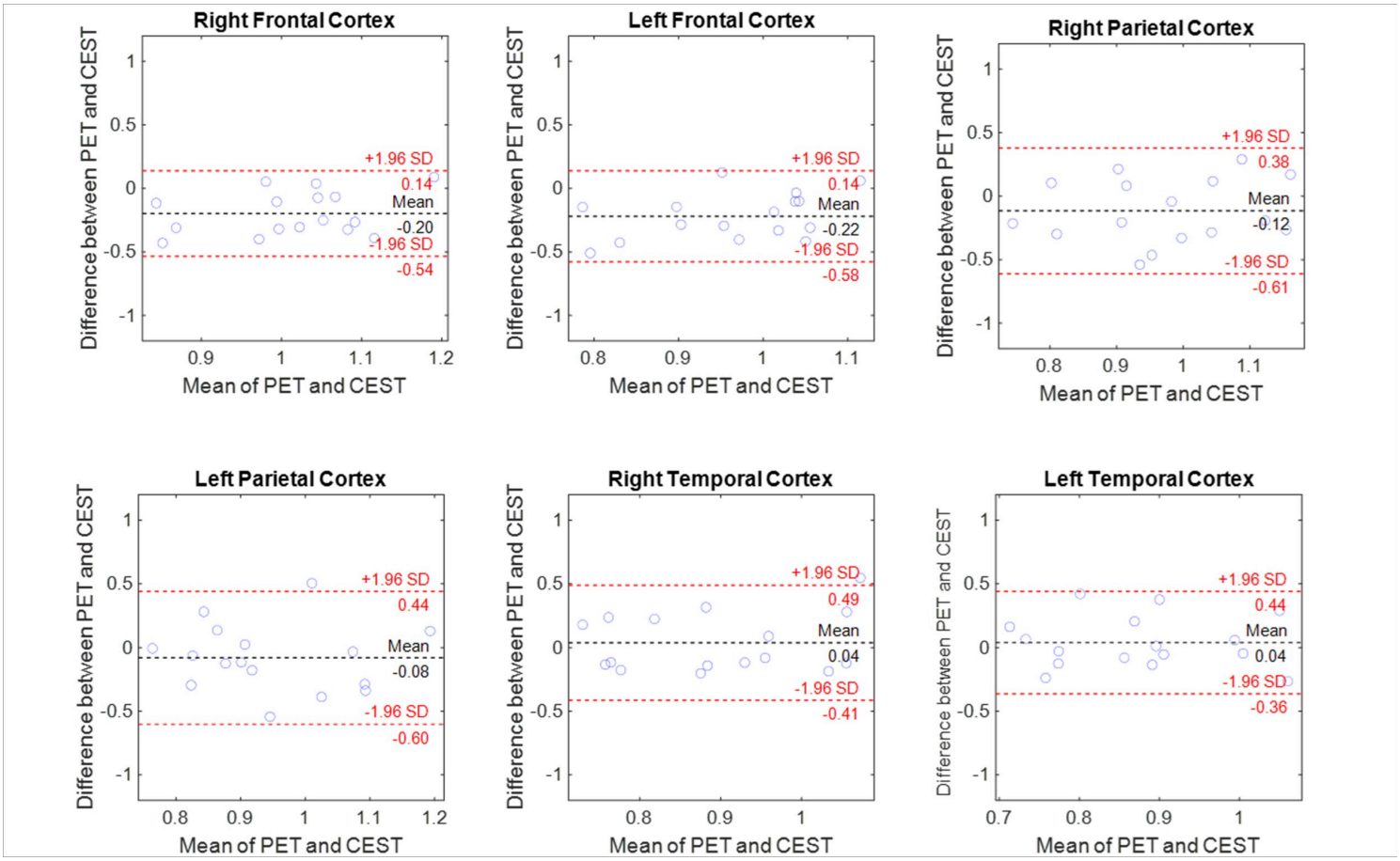


Figure 4

Bland-Altman plots between ^{18}F-FDG PET and glucoCEST measurements. Plots are shown for frontal, parietal, and temporal cortical regions in the left and right hemispheres. The difference between ^{18}F-FDG PET and glucoCEST values is plotted against their mean for each region. The black dashed line indicates the mean bias, and the red dashed lines represent the 95% limits of agreement (mean ± 1.96 SD). Each point represents an individual regional measurement from n = 16 patients with AD.

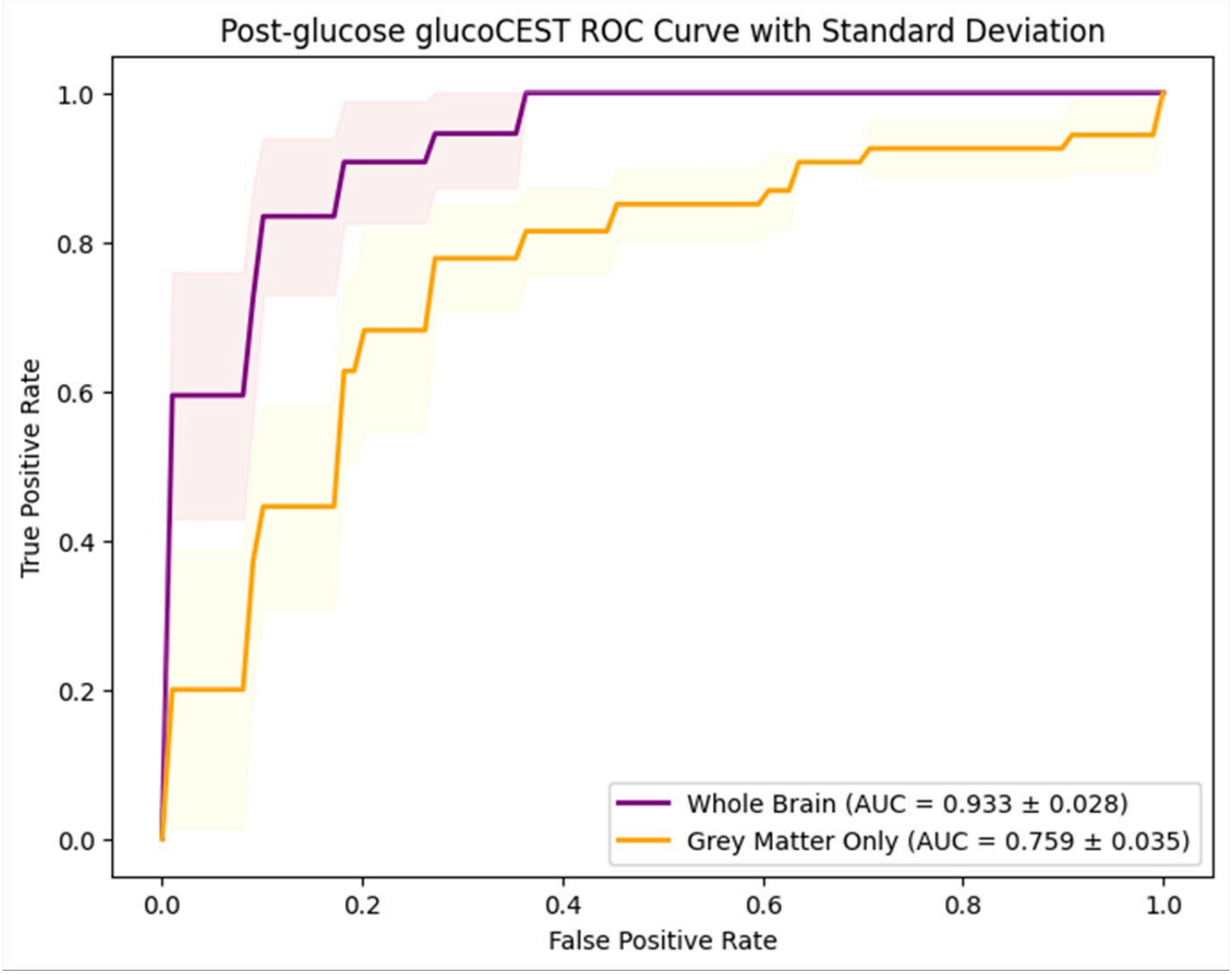


Figure 5

Receiver operating characteristic (ROC) curves demonstrating machine learning classification performance using post-glucose glucoCEST MRI features from whole-brain and GM-masked images. ROC curves are shown for the whole-brain model (purple line) and the GM-masked model (orange line). Models were trained and evaluated using data from n = 18 patients with AD and n = 18 cognitively healthy controls. The solid line represents the mean ROC curve obtained from stratified 5-fold cross-validation, and the shaded region indicates ± standard deviation across validation folds. The whole-brain model achieved an AUC of 0.934 ± 0.028, compared with 0.756 ± 0.035 for the GM-masked model.

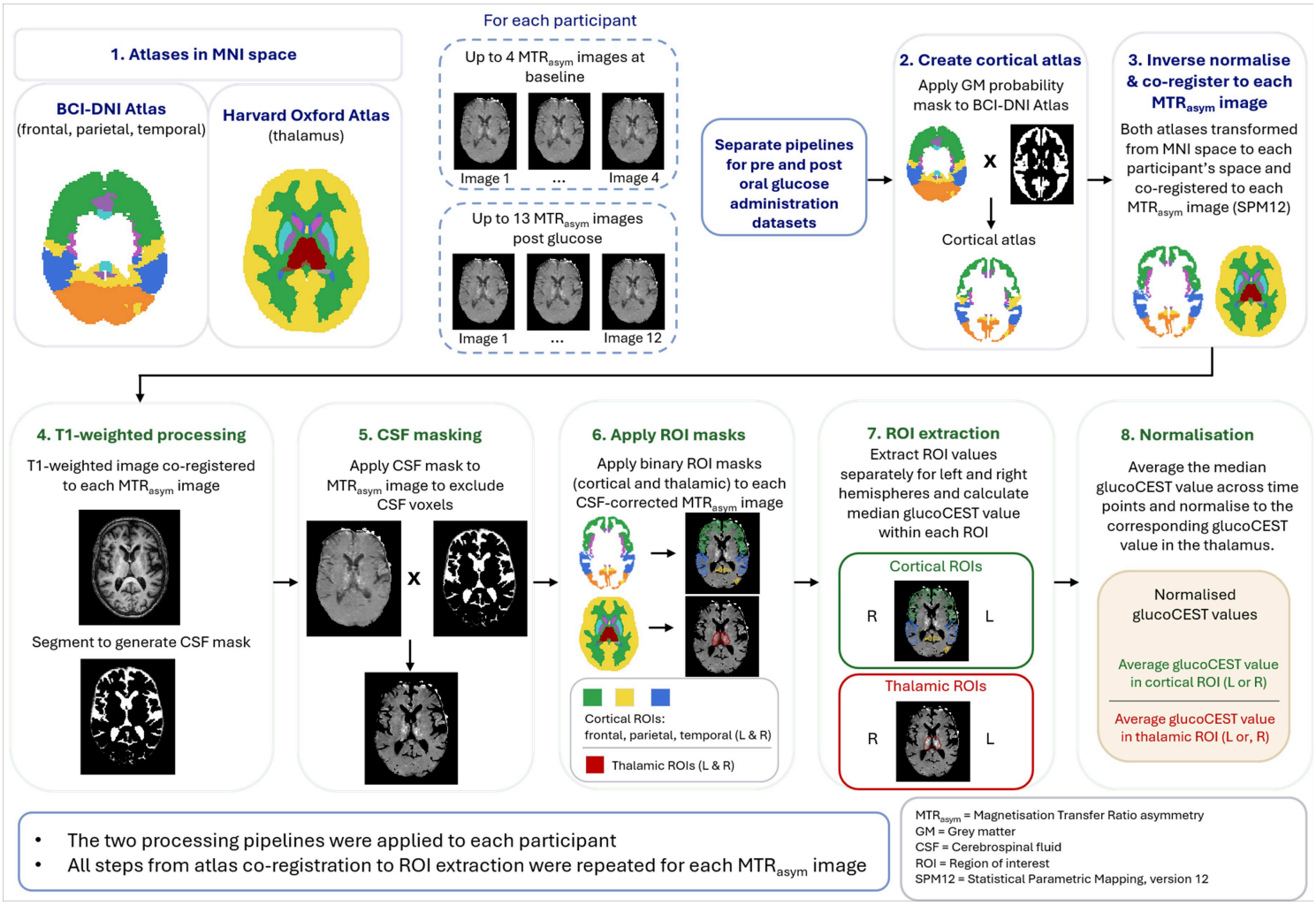


Figure 6

Flowchart of image processing pipeline for glucoCEST images. Anatomical atlases were transformed into individual image space and used for automated ROI definition. T_1-weighted images were co-registered to MTR_{asym} images, followed by CSF segmentation to exclude CSF voxels. Binary cortical and thalamic ROI masks were applied to CSF-corrected MTR_{asym} images, and median glucoCEST values were extracted from each ROI.

Supplementary Files

This is a list of supplementary files associated with this preprint. Click to download.

- SupplementaryMaterial.docx